



Cite this: *J. Mater. Chem. A*, 2016, **4**, 8172

Binding $\text{TiO}_2\text{-B}$ nanosheets with N-doped carbon enables highly durable anodes for lithium-ion batteries†

Chaoji Chen,^a Bao Zhang,^b Ling Miao,^b Mengyu Yan,^c Liqiang Mai,^c Yunhui Huang^{*a} and Xianluo Hu^{*a}

An effective strategy of binding $\text{TiO}_2\text{-B}$ nanosheets with N-doped carbon is developed to construct highly stable $\text{TiO}_2\text{-B}$ (001)|carbon interfaces with enhanced electronic conductivity and Li-uptake capability. The interfaces provide not only additional interfacial lithium-storage capability but also highly conductive pathways for the fast transport of electrons and lithium ions. The hybrid as an anode for lithium-ion batteries exhibits a safe operating potential window of ~ 1.5 V, superior rate capability with 180 mA h g^{-1} at 6 A g^{-1} , and ultra-long cycle life of more than 2000 cycles, holding great promise for safe and high-power energy storage applications.

Received 7th March 2016
Accepted 20th April 2016

DOI: 10.1039/c6ta01955b
www.rsc.org/MaterialsA

Introduction

The growing concerns on the consumption of non-renewable fossil fuels have driven people to explore renewable energy sources, including solar, water and wind powers for the past few decades. Meanwhile, the sustainable energy storage technology is vital for the application of renewable energy.^{1–3} Lithium-ion batteries (LIBs) represent one of the most vital and advanced technologies among all sustainable energy storage technologies, which is ascribed to their low environmental impact and high energy density.^{4,5} Despite the advances, there are still challenges in developing a suitable anode material with a relatively safe lithiation voltage, high power/energy density and long cycle life. It is known that the commercially used anode material, graphite, suffers from a severe safety problem arising from its ultralow lithiation voltage (near zero).⁶ $\text{Li}_4\text{Ti}_5\text{O}_{12}$ (LTO) that exhibits a lithiation voltage (towards lithium) of 1.55 V was found to be a candidate for solving the safety problem.^{7,8} Unfortunately, the capacity of LTO is only 170 mA h g^{-1} , which is a big limitation for its further application.

Recently, titanium oxide of the $\text{TiO}_2\text{-B}$ polymorph, discovered by Marchand *et al.*,⁹ has been the focus of many researchers as a high-power and high-capacity anode material because of its safer lithiation voltage relative to graphite,

acceptable capacity, high rate capability, structural stability over multiple cycles and low cost.^{10–20} Considering its comparable lithiation voltage (1.5 V) and the almost twice capacity (335 mA h g^{-1}) relative to LTO, there is no doubt that $\text{TiO}_2\text{-B}$ is much more attractive and suitable for next-generation LIBs with high power and energy densities. Nevertheless, there exist several disadvantages of using $\text{TiO}_2\text{-B}$ as anodes in LIBs. For instance, its poor electronic and ionic conductivity often limits the effective insertion/extraction of lithium into/out of the host structure. Meanwhile, the unstable cell structure or continuous side reactions between the electrode material and the electrolyte will cause unsatisfactory cyclability. Nanostructural design has been evidenced to be an effective strategy to address the issue of poor conductivity by shortening Li-diffusion pathways.^{10,11,15,17,20–22} However, nanostructuring also brings about lower volumetric energy density, severe side reactions and weaker adhesion between nanosized materials and current collectors, thus shortening the cycle life of LIBs. The formation of a stable solid electrolyte interface (SEI) film on the electrode material is believed to restrain the side reactions, which is beneficial to cycling stability.^{23,24} Besides, binder-free electrodes developed by Lou *et al.*¹² and Chen *et al.*¹³ are promising in achieving a long cycling life. The former retains 87% of capacity after 2000 cycles with a mass loading of 1.0 mg cm^{-2} in a carbon nanofiber-supported TiO_2 electrode, while the latter has a longer cycle life of 10 000 cycles with a much lower mass loading of 0.3 mg cm^{-2} in a Cu foil-supported TiO_2 electrode. In both cases, the tight adhesion between the active materials and the current collectors contributes to the cyclability. Moreover, pseudocapacitance arising from surface redox (de)lithiation or Li^+ intercalation characterizes a highly reversible capacity together with high power and energy densities.^{25,26} Inspired by this, to achieve long-life electrodes without sacrificing the mass

^aState Key Laboratory of Materials Processing and Die & Mould Technology, School of Materials Science and Engineering, Huazhong University of Science and Technology, Wuhan 430074, China. E-mail: huxl@mail.hust.edu.cn; huangyh@hust.edu.cn

^bWuhan National Laboratory for Optoelectronics, School of Optical and Electronic Information, Huazhong University of Science and Technology, Wuhan 430074, China

^cState Key Laboratory of Advanced Technology for Materials Synthesis and Processing, Wuhan University of Technology, Wuhan 430070, China

† Electronic supplementary information (ESI) available. See DOI: [10.1039/c6ta01955b](https://doi.org/10.1039/c6ta01955b)

loading, effective strategies may be focused on promoting pseudocapacitance, toughly adhering the active material to the current collector, and/or covering the active material with a stable SEI film.

Herein, we report an effective strategy of constructing a strongly coupled $\text{TiO}_2\text{-B}$ nanosheets/nitrogen-rich mesoporous carbon (NPC– $\text{TiO}_2\text{-B}$) composite to obtain a highly durable and high-rate anode for LIBs. The coupling between $\text{TiO}_2\text{-B}$ and the carbon matrix was confirmed by X-ray photoelectron spectroscopy (XPS) and electron paramagnetic resonance (EPR) measurements. Plenty of interfaces in the coupling region can offer additional lithium storage by enhancing the Li-uptake capability and electronic conductivity. This interfacial lithium storage combined with open tunnels in $\text{TiO}_2\text{-B}$ for fast Li-ion transport would contribute to capacitive charge, termed as pseudocapacitance, in the hybrid electrode. Moreover, the formation of a stable SEI film on the electrode material was further evidenced by a series of *ex situ* and *in situ* characterization techniques. In particular, the coupling between the $\text{TiO}_2\text{-B}$ nanosheets and the carbon microsheet of dozens of micrometers in width and length gives rise to a bulky architecture. It not only provides a three-dimensional (3D) conductive carbon network for the fast transport of electrons/ions and a reduced pathway for lithium insertion/extraction, but also offers a high packing density and strong adhesion between the electrode material and the current collector. Benefiting from these integrated advantages, a superior rate capability and ultra-long cycle life were obtained, without sacrificing the volumetric energy density and the active material mass loading, making this hybrid material highly attractive and suitable for long-life stationary energy storage applications.

Experimental

Materials synthesis

Nitrogen-rich mesoporous carbon (NPC) was synthesized on a large scale according to the literature.²⁷ In the synthesis of strongly coupled $\text{TiO}_2\text{-B}$ nanosheets/nitrogen-rich mesoporous carbon (NPC– $\text{TiO}_2\text{-B}$), 11 mg of NPC was added into the pre-mixed solution containing 15 mL of ethylene glycol (EG), 1 mL of H_2O , 1 mL of TiCl_3 (15 wt% in diluted HCl solution) and 60 μL of [Bmim][BF₄] ionic liquid under continuous stirring for 5 min and sonication for 30 min. The black suspension was sealed and treated under microwave irradiation at 160 °C for 30 min. The black powder was obtained after centrifugation, washed with water and ethanol several times and then dried at 80 °C for 24 h. $\text{TiO}_2\text{-B}$ nanosheets (TNSs) were prepared by a similar procedure to that of NPC– $\text{TiO}_2\text{-B}$ except using NPC. A physical mixture of NPC and TNSs was obtained by mechanically mixing NPC with TNSs (in a mass ratio of 86 : 14, named as NPC/TNS).

Materials characterization

The composition, microstructure, shape and size of the products were studied by scanning electron microscopy (SEM, SIRION200), transmission electron microscopy (TEM, JEOL JEM-2010F), powder X-ray diffraction (XRD, PANalytical B.V.,

Holland), XPS (VG MultiLab 2000 system with a monochromatic Al K α X-ray source, Thermo VG Scientific), and thermogravimetric (TG) analysis (from 50–850 °C with a heating rate of 10 °C min⁻¹). EPR measurements were carried out on a Bruker EMX spectrometer equipped with a cylindrical cavity operating at 100 kHz field modulation at 77 K. Raman and Fourier-transform infrared (FTIR) spectra were collected on a Renishaw inVia spectrometer with an Ar⁺ laser of 514.5 nm at room temperature.

Electrochemical measurements

The 2032 coin type cells were assembled for studying the electrochemical properties. A slurry of the active material, super P, and polyvinylidene fluoride (dissolved in *N*-methyl-2-pyrrolidone) in a mass ratio of 8 : 1 : 1 was coated onto a Cu foil as the working electrode. The mass loading of the active material is about 1.5–2 mg cm⁻². The lithium metal, Celgard 2300, and LiPF₆ (1 M) in a solvent (ethylene carbonate and dimethyl carbonate, 1 : 1 by volume) were used as the counter electrode, separator and electrolyte, respectively. Galvanostatic charge-discharge measurements were performed on a battery measurement system (Land, China) at different current densities over a potential ranging from 1 to 3 V. An electrochemical station (PARSTAT 2273 potentiostat) was utilized to investigate cyclic voltammetry (CV) and electrochemical impedance spectra (EIS) over the frequency range of 100 kHz to 0.01 Hz.

DFT calculation

The first-principles calculations are performed based on density functional theory (DFT) implemented in the VASP²⁸ package, and the electronic states were expanded using the projector augmented wave (PAW)²⁹ approach with a cutoff of 400 eV. The exchange-correlation energy is described by the functional of Perdew–Burke–Ernzerhof (PBE)³⁰ based on general gradient approximation (GGA). To model the $\text{TiO}_2\text{-B}|\text{NPC}$ interface, a 1 × 2 supercell of a partially –OH passivated $\text{TiO}_2\text{-B}$ (001) slab square lattice ($12.29 \times 7.55 \text{ \AA}$) with a thickness of 10 Å was used to match with the NPC square lattice with a 3 × 3 supercell ($12.78 \times 7.38 \text{ \AA}$). A vacuum thickness of 20 Å was set along the *c*-axis for the hybrid structure. The Brillouin zone is sampled with 3 × 5 × 1 Monkhorst mesh³¹ for the hybrid structure, and the force convergence thresholds are 0.05 eV Å⁻¹. Visualization of the structures is done using the VESTA software.

Results and discussion

NPC with a hard carbon structure, high-level N-doping (~7.7 wt%) and porous structure was synthesized according to the literature (Fig. S1†).²⁷ The NPC– $\text{TiO}_2\text{-B}$ hybrid was synthesized by a procedure described in the Experimental section. Briefly, a mixed dispersion containing NPC, EG, H_2O , TiCl_3 and [Bmim][BF₄] ionic liquid was sealed and treated under microwave irradiation at 160 °C for 30 min. After subsequent thermal treatment at 350 °C for 4 h to remove the residual organics, the final products were obtained. The observed and simulated XRD patterns of the NPC– $\text{TiO}_2\text{-B}$ hybrid with Rietveld refinement

confirm the phase structure of monoclinic $\text{TiO}_2\text{-B}$ in the $C2/m$ space group (JCPDF no. 74-1940) (Fig. 1a). It possesses a perovskite-like layered structure with open tunnels parallel to the b -axis, as illustrated in the inset of Fig. 1a. The Raman spectrum of the hybrid further evidences the formation of the $\text{TiO}_2\text{-B}$ polymorph, along with the existence of the carbon skeleton with D and G peaks (Fig. S2†). The carbon content in the hybrid can be evaluated to be about 14 wt% by TG analysis (Fig. S3†). SEM images display a bulky morphology of the hybrid, with dense tiny nanosheets (several nanometers in thickness) rooted on the micrometer sheets (dozens of micrometers in width and several micrometers in thickness) (Fig. S4†). TEM images further indicate the nanosheet-on-microsheet sandwich architecture (Fig. 1b). Clear lattices with a distance of 0.62 nm can be observed for an individual nanosheet, suggesting the phase structure of $\text{TiO}_2\text{-B}$ nanosheets (Fig. 1c). Furthermore, elemental mapping images of Ti, O, C and N elements demonstrate the uniform distribution of $\text{TiO}_2\text{-B}$ nanosheets that are not only on the surface of NPC but also inside its pore structure (inset in Fig. 1c). The nitrogen may be from the porous carbon matrix, as confirmed by the C 1s XPS result in Fig. 1f. As shown in Fig. 1e, the peak at 285.5 eV is assigned to the C–N bond, and N 1s peaks are assigned to pyridinic (N-6), pyrrolic (N-5) and quaternary (N-Q) nitrogen. A small peak at 283.5 eV related to the surface $\text{Ti}^{3+}\text{-C}$ or $\text{Ti}\text{-O-C}$ linkage can be observed in addition to the peaks at 284.5 eV (assigned to the elemental carbon/sp²-hybridized carbon from NPC), 286.5 eV (C–O bond) and 288.2 eV (C=O linkage), indicating the strong interaction

between titanium oxide and the carbon matrix.³² To further confirm the coupling effects of the NPC– $\text{TiO}_2\text{-B}$ hybrid, the EPR measurements were carried out. Results show that characteristic EPR resonances are hardly detectable for the $\text{TiO}_2\text{-B}$ nanosheets (TNSs) without coupling with NPC. In contrast, the NPC– $\text{TiO}_2\text{-B}$ hybrid exhibits an evident peak at $g = 1.945$, indicating the existence of surface Ti^{3+} (Fig. 1d).^{19,26} The integrated XPS and EPR results reveal a strong coupling between the carbon matrix and the tiny $\text{TiO}_2\text{-B}$ nanosheets.

The electrochemical performance of the NPC– $\text{TiO}_2\text{-B}$ hybrid was evaluated in a lithium half-cell. Fig. 2a presents the galvanostatic discharge/charge profiles of the NPC– $\text{TiO}_2\text{-B}| \text{Li}$ half-cell at a current density of 500 mA g⁻¹ for the initial 10 cycles. The discharge capacity slowly drops from 362 to 295 mA h g⁻¹, with an average voltage of 1.5 V. Excitingly, the NPC– $\text{TiO}_2\text{-B}$ electrode shows an impressive rate performance of 300, 245, 232, 210, 195 and 180 mA h g⁻¹ at 0.1, 0.2, 0.5, 1.5, 3.0 and 6 A g⁻¹, respectively (Fig. 2b). When the current density was reset to 0.1 A g⁻¹, a capacity of 260 mA h g⁻¹ can be obtained, indicating excellent reversibility of this electrode. Galvanostatic discharge/charge profiles from various current densities exhibit similar shapes, reflecting the structural stability of the host structure upon fast lithium insertion/extraction (Fig. 2c). A more intriguing feature of the NPC– $\text{TiO}_2\text{-B}$ electrode is the ultra-long cycling stability, as presented in Fig. 2d. Despite the slight drop of capacity before the initial dozens of cycles from 300 to 210 mA h g⁻¹, the capacity of subsequent cycles remains almost unchanged for more than 2200 cycles at a current density of

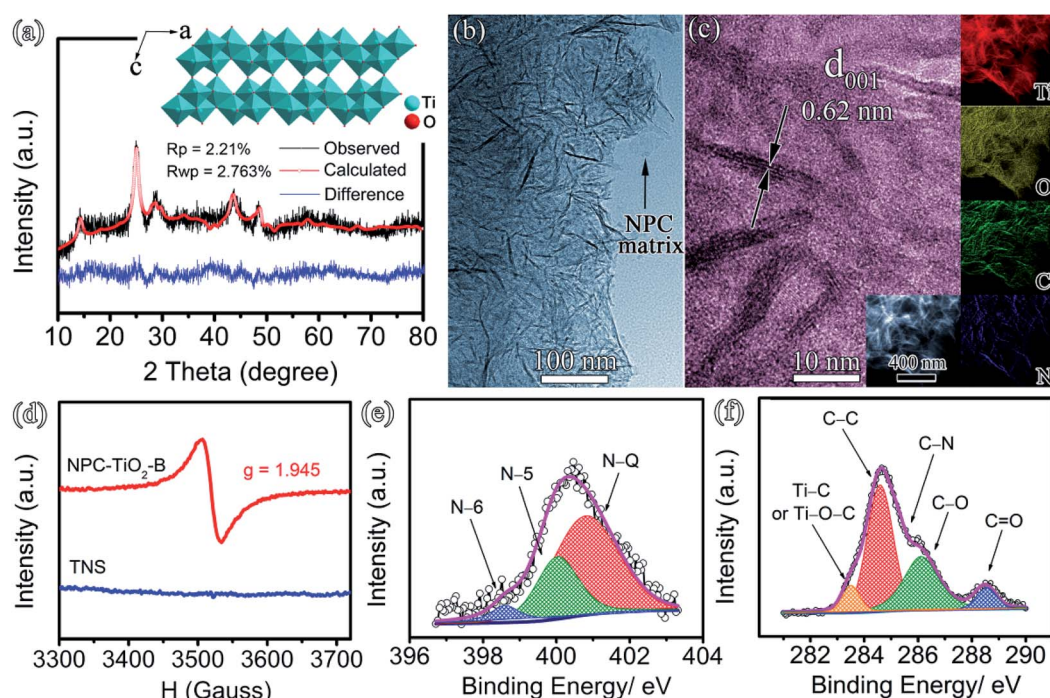


Fig. 1 (a) Observed and simulated XRD patterns of the NPC– $\text{TiO}_2\text{-B}$ product with Rietveld refinement. The inset shows the crystal structure of the $\text{TiO}_2\text{-B}$ viewed from the b -axis direction, lattice parameters in the $C2/m$ group, $a = 12.744(39)$ Å, $b = 3.738(09)$ Å, $c = 6.4435(28)$ Å, $\alpha = \gamma = 90^\circ$, $\beta = 100.481(4)$. (b and c) TEM and HR-TEM images of the NPC– $\text{TiO}_2\text{-B}$ product. (d) EPR spectra of the NPC– $\text{TiO}_2\text{-B}$ and TNS products. (e and f) High-resolution XPS spectra of N 1s and C 1s for the NPC– $\text{TiO}_2\text{-B}$ product. The inset in c shows the STEM image with the corresponding mapping images of Ti, O, C and N elements for the NPC– $\text{TiO}_2\text{-B}$ hybrid.

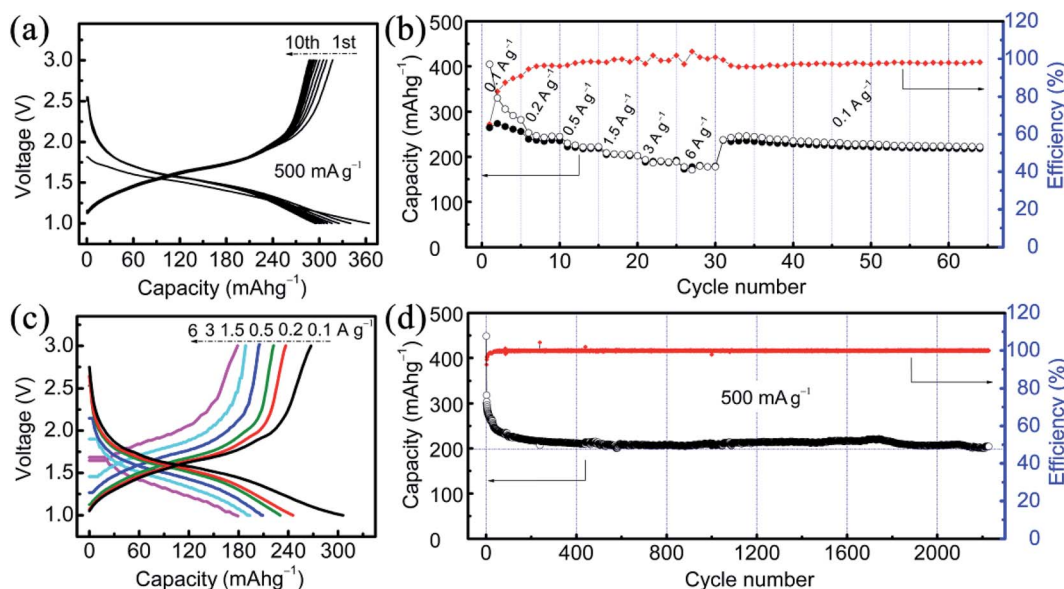


Fig. 2 Electrochemical lithium-storage performance of the NPC–TiO₂-B|Li half-cell: (a) discharge–charge profiles of the initial 10 cycles at 500 mA g^{−1}, (b) rate performance at different current densities, (c) discharge–charge profiles at different current densities, and (d) long-term cycling performance for 2230 cycles at 500 mA g^{−1}.

500 mA g^{−1} (~1.5C, 1C = 335 mA g^{−1}). Besides, the coulombic efficiency is stabilized at 100% after the initial 20 cycles. Despite the outstanding cyclability, it is noted that there exists irreversible capacity loss in the initial dozens of cycles, which mainly results from the irreversible side reaction between the surface –OH groups in the NPC–TiO₂-B hybrid and the carbonate-based electrolyte, as well as the irreversible trapping of lithium into the partial active sites of the NPC matrix. Previous work by Bruce *et al.*³³ has proven that the irreversible capacity loss in TiO₂-B based materials could be mitigated by appropriate surface treatment. More work in mitigating the irreversible capacity loss needs to be done in the near future. For comparison, the electrodes made of only TiO₂-B nanosheets (TNSs) or a physical mixture of TNSs and NPC (TNS/NPC) have also been investigated (see Fig. S5† for the morphologies of TNSs and NPC). Evidently, the two electrodes exhibit inferior cycling performances compared to the NPC–TiO₂-B electrode (Fig. S6†). The TNS electrode delivers a capacity of less than 80 mA h g^{−1} at 500 mA g^{−1} after 80 cycles. Although the TNS/NPC electrode shows an enhancement of 30 mA h g^{−1} in capacity compared to the TNS electrode, its electrochemical performance is still unsatisfactory. On one hand, the low intrinsic conductivity of TiO₂-B and their agglomeration may result in inferior performances. On the other hand, the physical mixture of TNSs and NPC could not significantly favor the total conductivity of the mixture, due to the loose contact and additional resistance.

To get further insight into the outstanding rate capability and ultra-long cycling life of the hybrid electrode, we have performed several analysis methods utilizing various characterization techniques combined with first principles calculations. First, we have performed CV measurements to explore the electrochemical kinetics of lithium insertion/extraction,

especially to distinguish the capacitive charge from solid-state diffusion. Fig. 3a shows the initial four cycles of CV curves at a scan rate of 0.2 mV s^{−1}. Two pairs of redox peaks at 1.5/1.55 V (S₁ peak) and 1.6/1.65 V (S₂ peak) can be observed, accompanied by a pair of weak redox peaks at 1.75/2.0 V (A peak). It is generally believed that the S peaks are related to the pseudo-capacitive behavior of lithium in TiO₂-B, whereas the A peaks are assigned to the solid-state diffusion of lithium in anatase.^{34–36} The overlap of CV curves from 3 to 4 cycles indicates the high reversibility of the hybrid electrode. When increasing the scan rates from 0.1 to 2.0 mV s^{−1} (Fig. 3b), the CV

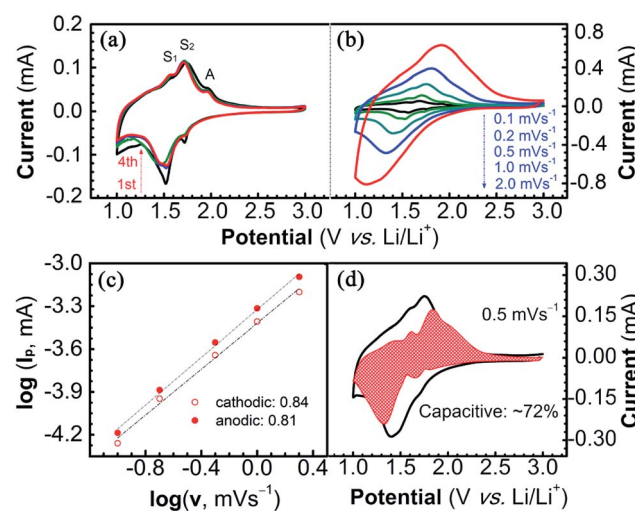


Fig. 3 Kinetic analysis of the NPC–TiO₂-B electrode: (a) 1st–4th cycles at 0.2 mV s^{−1}, (b) CV curves at various scan rates, (c) relationship between the log(scan rate, v) and the log(peak current, I_p), and (d) capacitive charge at a scan rate of 0.5 mV s^{−1}.

Published on 21 April 2016. Downloaded by WUHAN UNIVERSITY OF TECHNOLOGY on 29/03/2017 10:20:47.

curves show similar shapes despite an increase of peak separations as the scan rates get higher, reflecting the higher overpotentials necessary to deliver larger currents. It is noteworthy that the A peaks become increasingly weaker as the scan rates increase and become undistinguished at 1.0 mV s^{-1} , indicating the limitation of the solid-state diffusion process in anatase at high rates due to the slow kinetics of this process.

The charge contributions from the two distinct processes, fast capacitive-controlled reaction (proportional to scan rate ν) and slow solid-state diffusion insertion-controlled reaction (proportional to scan rate $\nu^{-1/2}$), can be determined according to the relationship of $i = av^b$,^{37–39} where i is the total current, ν refers to the scan rate, and a and b are two adjustable parameters. A b -value of 1 indicates that the charge contribution is totally from the capacitive-controlled reaction, whereas 0.5 means that the charge is totally contributed by the diffusion insertion-controlled reaction. By plotting the $\log(\text{scan rate } \nu) - \log(\text{peak current } I_p)$ diagram, the b -value can be determined by the value of the slope. As presented in Fig. 3c, b -values of 0.84 and 0.81 from the cathodic/anodic processes, respectively, can

be obtained. The relatively high values close to 1 indicate that the electrochemical behavior of lithium in the hybrid electrode is capacitive-dominated along with a minor contribution from the solid-state diffusion process. More specifically, by using Dunn's method,^{25,38,39} it is possible to quantify the exact contributions from the two distinct processes (see ESI S1† for more calculation details). Accordingly, at a scan rate of 0.5 mV s^{-1} , the capacitive contribution is calculated to be $\sim 72\%$ (Fig. 3d), consistent with the above analysis.

From a structural point of view, the capacitive-dominated electrochemical behavior may be contributed to the unique open tunnels in the $\text{TiO}_2\text{-B}$ crystal structure and the interfacial lithium storage at the $\text{NPC}|\text{TiO}_2\text{-B}$ interfaces. The open tunnels along the b - and c -axes in $\text{TiO}_2\text{-B}$ provide facile 2D Li-ion diffusion pathways that conduce the charge storage to behave in a quasi-2D process, similar to the 2D surface adsorption reactions.^{36,40–42} On the other hand, the coupling between the $\text{TiO}_2\text{-B}$ nanocrystals and the carbon matrix introduces plenty of interfaces where additional lithium storage may occur considering the enhanced Li-uptake capability and electronic conductivity.

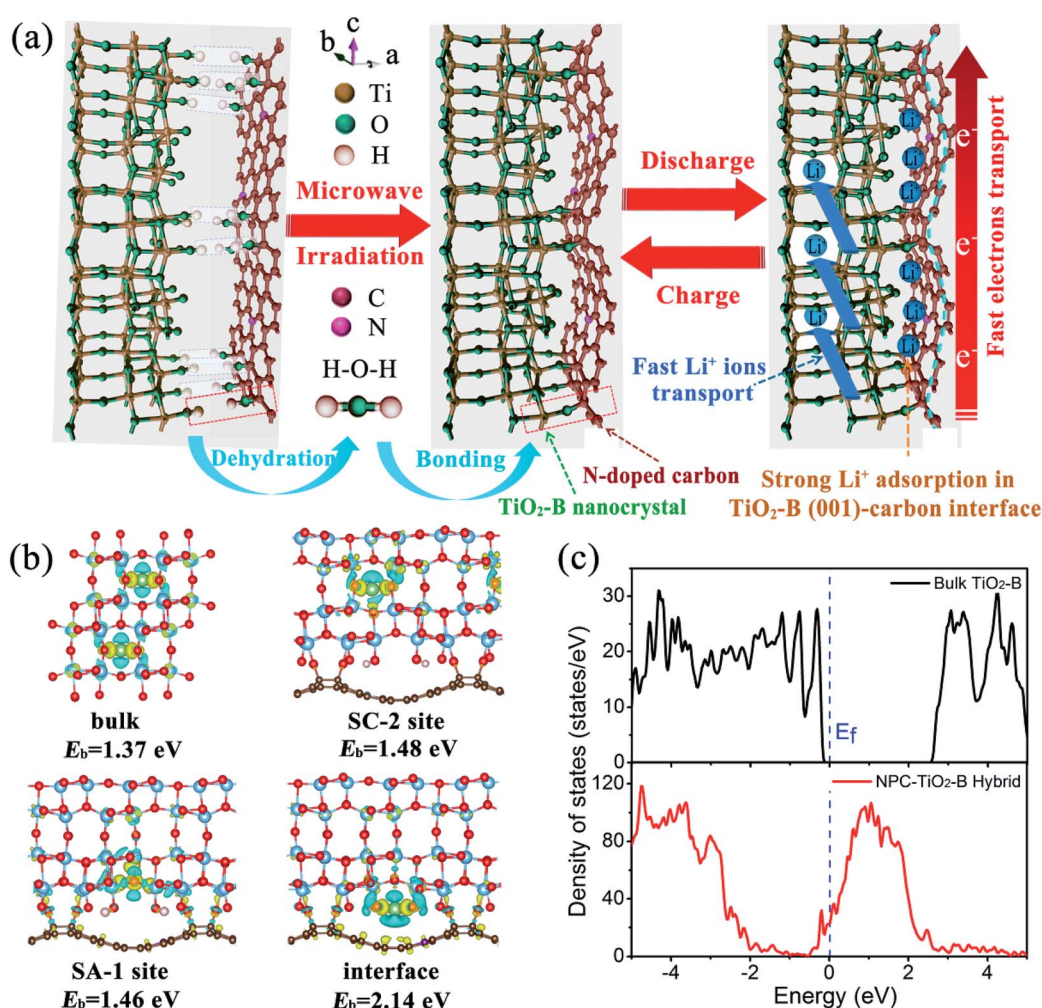


Fig. 4 (a) Illustration of the coupling process between the $\text{TiO}_2\text{-B}$ and N-doped carbon matrix. (b) Isosurface (yellow for $\Delta\rho > 0$ and blue for $\Delta\rho < 0$) of the difference charge density ($\Delta\rho$) for the most stable configuration of Li-uptake on various sites of bulk $\text{TiO}_2\text{-B}$ and the NPC– $\text{TiO}_2\text{-B}$ hybrid and the corresponding binding energies (E_b) with Li atoms. (c) Simulations of the density of states for bulk $\text{TiO}_2\text{-B}$ and the NPC– $\text{TiO}_2\text{-B}$ hybrid.

Fig. 4a graphically illustrates the coupling process (I-II), which is driven by the interactions between the surface -OH groups of $\text{TiO}_2\text{-B}$ and carbon matrix through a dehydration reaction ($\text{Ti-OH} + \text{HO-C} \rightarrow \text{Ti-O-C} + \text{H}_2\text{O}$) and the integrated lithium-storage behaviors of Li^+ insertion/extraction in the $\text{TiO}_2\text{-B}$ host structure and interfacial lithium storage occurring at the $\text{NPC}|\text{TiO}_2\text{-B}$ interface (III).

Furthermore, we have performed first principles calculations on the Li-uptake capability and electronic conductivity for the interface of the NPC-TiO₂-B hybrid. The Li uptake on the hybrid structure compared with that on bulk TiO₂-B (1 × 2 × 1 supercell) is considered. The stability of Li uptake can be measured by the binding energy (higher value means more stable), given as $E_b = E_s + E_{\text{Li}} - E_a$, where E_s , E_a and E_{Li} represent the total energies of the total structure after Li uptake, the NPC-TiO₂-B hybrid or bulk TiO₂-B and isolated Li^+ ions, respectively. Fig. 4b shows the isosurface (yellow for $\Delta\rho > 0$ and blue for $\Delta\rho < 0$) of the difference charge density ($\Delta\rho$) for the most stable configuration of different uptake sites of Li^+ ions in bulk TiO₂-B and the NPC-TiO₂-B hybrid, and the corresponding binding energies (E_b). The binding energies at SC2 and SA1 sites of the hybrid structure are about 1.48 and 1.46 eV, a little higher than that in bulk TiO₂-B (1.37 eV). More excitingly, the binding energy of Li^+ ions at the interface can reach 2.14 eV, indicating that the Li-uptake capability at the interface is much enhanced. Thus, the synergistic interaction of the TiO₂-B nanosheets and the carbon matrix makes the Li uptake at the interface more stable and avoids the formation of dendrites upon cycling. To explore the coupling effects on the electronic conductivity in the NPC-TiO₂-B hybrid, the density of states (DOS) for the bulk TiO₂-B and the NPC-TiO₂-B hybrid has been calculated. Surprisingly, the hybrid structure exhibits a much narrower band gap (~0 eV) towards raw TiO₂-B (~2.4 eV) with some impurity signals near the Fermi-level, both indicating an improved electronic conductivity of the hybrid structure. Here, the strong coupling between the TiO₂-B nanocrystals and the carbon matrix enhances not only the Li-uptake capability but also the electronic conductivity, both of which contribute to the

superior rate capability and long-term cyclability of the hybrid electrode. The much higher conductivity of the hybrid than that of raw TiO₂-B indicates that the internal resistance of the hybrid electrode would be much lower than that of the TNS electrode, which agrees well with the electrochemical impedance spectrum (EIS) results (Fig. S7†).

Trying to get further understanding on the outstanding long-term cyclability of the hybrid electrode, we have investigated the surface states of the electrode during the electrochemical lithiation/delithiation processes. The NPC-TiO₂-B|Li cells were disassembled at different states-of-charge in the initial cycle, and Fourier-transform infrared (FTIR) spectra were collected (Fig. 5a). As the voltage decreases upon discharge, the peaks associated with vibrations involving $\nu(\text{C=O})$, $\nu(\text{C-O})$, $\nu(\text{P=O})$, $\nu(\text{P-O-C})$, $\delta(\text{OCO}_2)$ and $\delta(\text{C-H})$ are increased, which is similar to the previous reports on the SEI films on the electrode surfaces including carbon, Li metal and metal oxides.³³ The SEI film was generated on the electrode, involving Li-containing carbonate and Li_2CO_3 resultants from solvent decomposition, and organic phosphate products from hydrolyzation of the PF_6^- groups.³³ The *ex situ* O 1s XPS results have also confirmed the formation of Li-containing carbonate and Li_2CO_3 upon discharge that are related to the SEI film (Fig. 5b), while the *ex situ* Ti 2p XPS results evidenced the redox reactions between $\text{Ti}^{4+}/\text{Ti}^{3+}$ (Fig. S8†). *In situ* EIS results for the initial discharge-charge cycle and the 20 and 100th cycle are presented in Fig. 6. Upon discharging, the semi-circles assigned to the Li^+ diffusion in the surface film at high frequency show a decreasing trend in diameter, indicating a dropping trend of resistance towards Li^+ insertion into the film and the electrode materials (Fig. 6a). It may be assigned to the distinct transport properties of Li^+ ions in the as-formed surface film. In the subsequent charge and cycling processes (20th, 100th cycle, Fig. 6b), the EIS spectra finally reach a steady state, suggesting the formation of a stable SEI film.

Besides, we have also investigated the stability of the electrode after 2230 cycles of charging-discharging. The adhesion between the electrode material and the current collector is

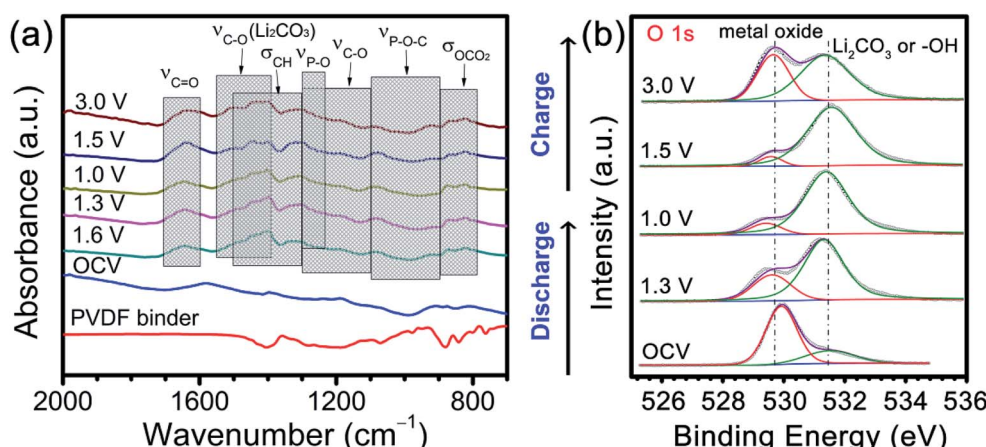


Fig. 5 *Ex situ* FTIR spectra (a) and high-resolution XPS spectra of O 1s (b) for the NPC-TiO₂-B electrodes at various states of discharge then charge. Special regions assigned to the particular functional group vibrations are highlighted by dashed rectangles.

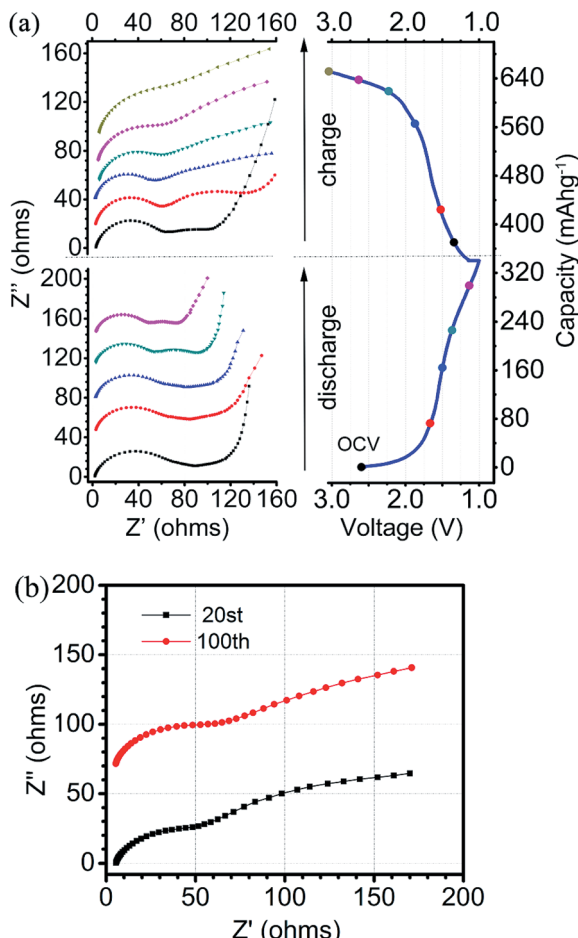


Fig. 6 (a) *In situ* EIS spectra of the NPC–TiO₂-B electrode at various charged/discharged states and the corresponding charge-discharge profiles. (b) Comparison of the EIS spectra for the NPC–TiO₂-B electrode after 20 and 100 cycles.

highly stable, remaining tightly connected even after 2230 cycles (Fig. 7a–c). The TEM image confirms the excellent stability of the NPC–TiO₂-B hybrid microstructure, while the

HR-TEM image along with the selected-area electron diffraction (SAED) pattern reveals that the crystal structure of the TiO₂-B nanosheets retains well (Fig. 7d and e). The excellent stability of the NPC–TiO₂-B electrode should be ascribed to the bulky architecture of the hybrid as well as the strong coupling between the TiO₂-B nanocrystals and the carbon matrix. In a word, the formation of a stable SEI film on the surface of the electrode materials along with the excellent stability of the electrode structure contributes to the superior durability of the NPC–TiO₂-B hybrid electrode, enabling an attractive alternative in the field of low-cost and large-scale energy storage applications.

Conclusions

In summary, we have developed an effective strategy of binding TiO₂-B nanosheets with nitrogen-rich carbon to achieve a high-rate (180 mA h g⁻¹ at 6 A g⁻¹) and highly durable (more than 2000 cycles) anode material for LIBs. Further kinetic analysis based on the CV technique reveals a capacitive-dominated charging process in the hybrid electrode, benefitting from the facile 2D channels along the *b*- and *c*-axes in the TiO₂-B host structure for fast Li-ion transport as well as the interfacial lithium-storage occurring at the coupled NPC|TiO₂-B interface. Further simulated results based on first principles calculations reveal that the strong coupling between the TiO₂-B nanocrystals and the carbon matrix enhances not only the Li-uptake capability but also the electronic conductivity of the hybrid. Besides, monitoring of the surface states of the hybrid electrodes upon discharging-charging by *ex situ* FTIR/XPS and *in situ* EIS shows that a stable SEI film is formed on the electrode surface, leading to an ultra-long cycle life. Our work demonstrates that the NPC–TiO₂-B hybrid is promising as a high-rate and long-life anode for sustainable energy storage. We also believe that the coupling strategy between TiO₂-B and the carbon matrix as well as the powerful analysis methods would offer guidelines for optimized battery performances in other hybrid electrode systems.

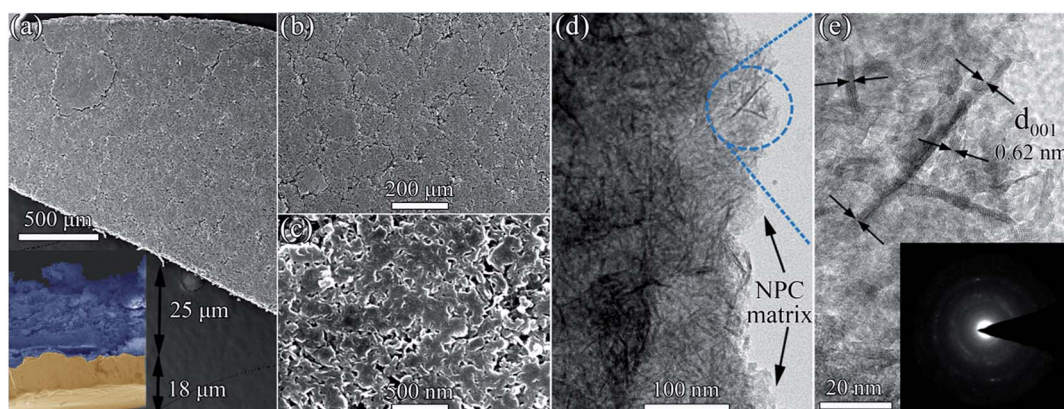


Fig. 7 Structural characterization of the NPC–TiO₂-B electrode after 2230 cycles. (a–c) SEM images, inset is the SEM image of the cross-section of the electrode; (d) TEM image; (e) HR-TEM image, inset is the SAED pattern of the electrode.

Acknowledgements

This work is supported by the National High-tech R&D Program of China (863 Program, No. 2015AA034601), and National Natural Science Foundation of China (No. 51522205, 51472098 and 21271078), and Program for New Century Excellent Talents in University (No. NECT-12-0223).

Notes and references

- 1 M. Armand and J. M. Tarascon, *Nature*, 2008, **451**, 652–657.
- 2 B. Dunn, H. Kamath and J. M. Tarascon, *Science*, 2011, **334**, 928–935.
- 3 J. Liu, J. G. Zhang, Z. G. Yang, J. P. Lemmon, C. Imhoff, G. L. Graff, L. Y. Li, J. Z. Hu, C. M. Wang, J. Xiao, G. Xia, V. V. Viswanathan, S. Baskaran, V. Sprenkle, X. L. Li, Y. Y. Shao and B. Schwenzer, *Adv. Funct. Mater.*, 2013, **23**, 929–946.
- 4 J. B. Goodenough and K. S. Park, *J. Am. Chem. Soc.*, 2013, **135**, 1167–1176.
- 5 P. G. Bruce, B. Scrosati and J.-M. Tarascon, *Angew. Chem., Int. Ed.*, 2008, **47**, 2930–2946.
- 6 D. Aurbach, E. Zinigrad, Y. Cohen and H. Teller, *Solid State Ionics*, 2002, **148**, 405–416.
- 7 L. F. Shen, E. Uchaker, X. G. Zhang and G. Z. Cao, *Adv. Mater.*, 2012, **24**, 6502–6506.
- 8 J. H. Liu, J. S. Chen, X. F. Wei, X. W. Lou and X. W. Liu, *Adv. Mater.*, 2011, **23**, 998–1002.
- 9 R. Marchand, L. Brohan and M. Tournoux, *Mater. Res. Bull.*, 1980, **15**, 1129–1133.
- 10 A. R. Armstrong, G. Armstrong, J. Canales and P. G. Bruce, *Angew. Chem., Int. Ed.*, 2004, **43**, 2286–2288.
- 11 Y. Ren, Z. Liu, F. Pourpoint, A. R. Armstrong, C. P. Grey and P. G. Bruce, *Angew. Chem., Int. Ed.*, 2012, **51**, 2164–2167.
- 12 S. H. Liu, Z. Y. Wang, C. Yu, H. B. Wu, G. Wang, Q. Dong, J. S. Qiu, A. Eychmüller and X. W. Lou, *Adv. Mater.*, 2013, **25**, 3462–3467.
- 13 Y. X. Tang, Y. Y. Zhang, J. Y. Deng, J. Q. Wei, H. L. Tam, B. K. Chandran, Z. L. Dong, Z. Chen and X. D. Chen, *Adv. Mater.*, 2014, **26**, 6111–6118.
- 14 H. S. Liu, Z. H. Bi, X. G. Sun, R. R. Unocic, M. P. Paranthaman, S. Dai and G. M. Brown, *Adv. Mater.*, 2011, **23**, 3450–3454.
- 15 S. H. Liu, H. P. Jia, L. Han, J. L. Wang, P. F. Gao, D. D. Xu, J. Yang and S. N. Che, *Adv. Mater.*, 2012, **24**, 3201–3204.
- 16 H. Hu, L. Yu, X. H. Gao, Z. Lin and X. W. Lou, *Energy Environ. Sci.*, 2015, **8**, 1480–1483.
- 17 M. Sondergaard, K. J. Dalgaard, E. D. Bojesen, K. Wonsyld, S. Dahl and B. B. Iversen, *J. Mater. Chem. A*, 2015, **3**, 18667–18674.
- 18 C. J. Chen, X. L. Hu, Z. H. Wang, X. Q. Xiong, P. Hu, Y. Liu and Y. H. Huang, *Carbon*, 2014, **69**, 302–310.
- 19 V. Etacheri, J. E. Yourey and B. M. Bartlett, *ACS Nano*, 2014, **8**, 1491–1499.
- 20 Q. L. Wu, J. G. Xu, X. F. Yang, F. Q. Lu, S. M. He, J. L. Yang, H. J. Fan and M. M. Wu, *Adv. Energy Mater.*, 2015, **5**, 1401756.
- 21 M. S. Wang, W. L. Song and L. Z. Fan, *J. Mater. Chem. A*, 2015, **3**, 12709–12717.
- 22 L. Z. Fan, S. S. Chi, L. N. Wang, W. L. Song, M. He and L. Gu, *ChemElectroChem*, 2015, **2**, 421–426.
- 23 H. Nakai, T. Kubota, A. Kita and A. Kawashima, *J. Electrochem. Soc.*, 2011, **158**, A798–A801.
- 24 L. Ji, M. Gu, Y. Shao, X. Li, M. H. Engelhard, B. W. Arey, W. Wang, Z. Nie, J. Xiao, C. Wang, J.-G. Zhang and J. Liu, *Adv. Mater.*, 2014, **26**, 2901–2908.
- 25 V. Augustyn, J. Come, M. A. Lowe, J. W. Kim, P.-L. Taberna, S. H. Tolbert, H. D. Abruna, P. Simon and B. Dunn, *Nat. Mater.*, 2013, **12**, 518–522.
- 26 C. J. Chen, Y. W. Wen, X. L. Hu, X. L. Ji, M. Y. Yan, L. Q. Mai, P. Hu, B. Shan and Y. H. Huang, *Nat. Commun.*, 2015, **6**, 6929.
- 27 L. Qie, W. M. Chen, H. H. Xu, X. Q. Xiong, Y. Jiang, F. Zou, X. L. Hu, Y. Xin, Z. L. Zhang and Y. H. Huang, *Energy Environ. Sci.*, 2013, **6**, 2497–2504.
- 28 G. Kresse and J. Hafner, *Phys. Rev. B: Condens. Matter Mater. Phys.*, 1994, **49**, 14251–14269.
- 29 G. Kresse and D. Joubert, *Phys. Rev. B: Condens. Matter Mater. Phys.*, 1999, **59**, 1758–1775.
- 30 J. P. Perdew, K. Burke and M. Ernzerhof, *Phys. Rev. Lett.*, 1996, **77**, 3865–3868.
- 31 H. J. Monkhorst and J. D. Pack, *Phys. Rev. B: Solid State*, 1976, **13**, 5188–5192.
- 32 Q. Huang, S. Tian, D. Zeng, X. Wang, W. Song, Y. Li, W. Xiao and C. Xie, *ACS Catal.*, 2013, **3**, 1477–1485.
- 33 S. Brutti, V. Gentili, H. Menard, B. Scrosati and P. G. Bruce, *Adv. Energy Mater.*, 2012, **2**, 322–327.
- 34 C. J. Chen, X. L. Hu, Y. Jiang, Z. Yang, P. Hu and Y. H. Huang, *Chem.–Eur. J.*, 2014, **20**, 1383–1388.
- 35 M. Zukalová, M. Kalbac, L. Kavan, I. Exnar and M. Graetzel, *Chem. Mater.*, 2005, **17**, 1248–1255.
- 36 A. G. Dylla, G. Henkelman and K. J. Stevenson, *Acc. Chem. Res.*, 2013, **46**, 1104–1112.
- 37 H. Lindström, S. Södergren, A. Solbrand, H. Rensmo, J. Hjelm, A. Hagfeldt and S.-E. Lindquist, *J. Phys. Chem. B*, 1997, **101**, 7717–7722.
- 38 J. Wang, J. Polleux, J. Lim and B. Dunn, *J. Phys. Chem. C*, 2007, **111**, 14925–14931.
- 39 D. F. Xu, C. J. Chen, J. Xie, B. Zhang, L. Miao, J. Cai, Y. H. Huang and L. N. Zhang, *Adv. Energy Mater.*, 2016, **6**, 1501929.
- 40 Z. Liu, Y. G. Andreev, A. Robert Armstrong, S. Brutti, Y. Ren and P. G. Bruce, *Phys. Rev. B: Condens. Matter Mater. Phys.*, 2013, **23**, 235–244.
- 41 C. J. Chen, X. L. Hu, B. Zhang, L. Miao and Y. H. Huang, *J. Mater. Chem. A*, 2015, **3**, 22591–22598.
- 42 C. J. Chen, X. L. Hu, P. Hu, Y. Qiao, L. Qie and Y. H. Huang, *Eur. J. Inorg. Chem.*, 2013, **2013**, 5320–5328.
- 43 R. Demir-Cakan, M. Morcrette, G. Babu, A. Gueguen, R. Dedryvere and J.-M. Tarascon, *Energy Environ. Sci.*, 2013, **6**, 176–182.